

Nonlinear Rotordynamic Computations of Automotive Turbochargers Using Rotating Floating Ring Bearings at High Rotor Speeds

Hung Nguyen-Schäfer

Bosch Mahle Turbo Systems (BMTS), Germany
hung.nguyen-schaefer@bmturbosystems.com

Abstract

Nonlinear rotor responses of an automotive turbocharger using two separate rotating floating ring bearings at the run-up simulation to nearly 230,000 rpm have been carried out. Due to nonlinearity of the oil film bearings, the rotordynamic behavior of the turbocharger becomes more nonlinear at increasing rotor speeds. Some non-synchronous responses of the rotor, such as the inner and outer oil whirls are induced besides the synchronous response of the rotor unbalance. The nonlinear bearing forces, ring speed ratio of the bearing, damping effect of the seal rings, and gyroscopic effects of the compressor and turbine wheels are taken into account in the rotordynamic computation. A two-phase oil film flow in the bearing clearances is used to compute the nonlinear bearing forces at each integration time step by the impedance method that is resulted from solving the two-phase Reynolds lubrication equation. The flexible rotor vibration modes and rotor orbits at various positions of the rotor are displayed in the 3-D displacement plots and phase planes, respectively. The computational results are shown and analyzed in Waterfall plots in which the frequency spectra of the synchronous and subsynchronous rotor responses of the inner and outer oil whirls are displayed and compared with measurements. This gives a deeper understanding of the rotor responses for further developments of rotordynamics and bearing system of automotive turbochargers.

Keywords: turbochargers; downsizing engines; rotating floating ring bearings; two-phase flows; inner and outer oil whirls; oil whip; induced noises; unbalance whistle; constant tone; harmonic and subsynchronous vibration responses; self-excited subsynchronous vibrations.

1 Introduction

In automotive turbochargers, the excited unbalance forces at high rotor speeds are much larger than the rotor weights on the order of approximately 10^2 according to [2]. As a reason, the journal moves from the bearing center outwards to the bearing wall due to the large unbalance force at increasing rotor speeds. At high rotor speeds, the bearing stiffness and damping coefficients strongly increase; therefore, the journal orbit moves towards the bearing center and is stabilized in the limit cycle resulting from Hopf bifurcation. This indicates that the turbocharger journal moves nearly the entire bearing clearance in the rotor speed range. The nearer to the bearing wall the journal moves, the more nonlinear the bearing characteristics, such as bearing stiffness and damping coefficients; therefore, the rotordynamic behavior of the turbocharger becomes more and more nonlinear. Some non-synchronous responses of the rotor are induced by superimposing the harmonic unbalance excitation on the subsynchronous components of the nonlinear rotor system, such as inner and outer oil whirl vibrations besides synchronous unbalance response of the rotor [2, 3].

2 Nonlinear Rotordynamic Computations of Automotive Turbochargers

2.1 Vibration Equations of a Turbocharger Rotor

Figure 1 displays the rotor of an automotive turbocharger in the CHRA (Center Housing and Rotating Assembly) including the rotor shaft, compressor wheel, turbine wheel, rotating floating ring bearings (RFRBs), seal rings, and thrust rings. All components must be taken into account in the rotordynamic computation to study

the rotor vibration response, such as the frequency components in the Waterfall plot, shaft orbit in the phase plane, and rotor amplitude of the response vibrations in the time domain plots.

The continuum vibration equations of the rotor are usually discretized by two methods, the finite element and transfer matrix methods. The *finite element method*, a discretization method of the continuum structure of the rotor, is based on the principle of D'Alembert in which the sum of virtual work of all rotor elements equals zero. By discretization of the continuum vibration equations, one divides the rotor into a finite number of elements in the computational model including concentrated masses, cylindrical elements, disks, and interfaces between the rotor, bearings, and seal rings. Therefore, the rotor vibration equations are derived and written in a discrete matrix equation. Another alternative method is the *transfer matrix method* developed by Myklestad and Prohl in which the first element of the rotor is connected with the last one by the overall-transfer matrix that consists of the transfer matrices of all rotor elements. The main advantage of this second method is to spare the computational working memory compared to the finite element method.

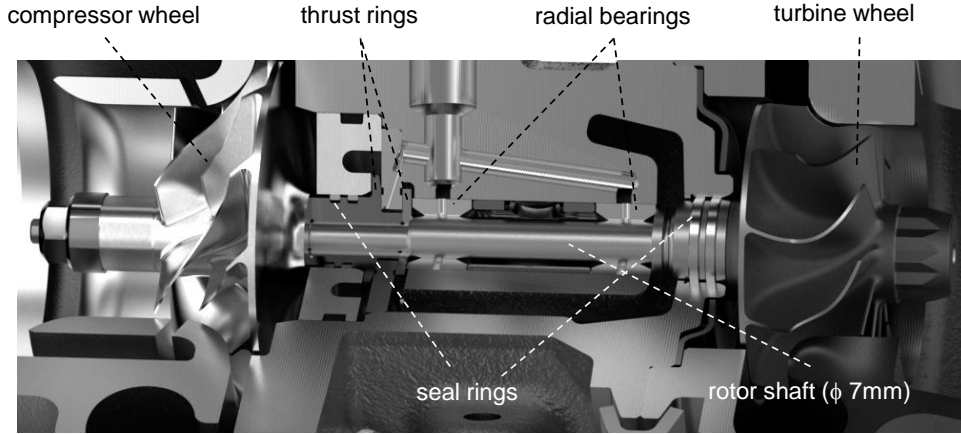


Figure 1: Automotive turbocharger rotor setup in the CHRA [2]

The vibration equations of the rotor with N degrees of freedom (DOF), as shown in Fig. 1 are written in the discrete matrix equation of

$$\mathbf{M}\ddot{\mathbf{x}} + \mathbf{C}_{SG}\dot{\mathbf{x}} + \mathbf{K}_S\mathbf{x} = \mathbf{f}(\mathbf{t}) \quad (1)$$

where

$\mathbf{M} = (N \times N)$ mass matrix containing the masses and inertia moments of the rotor with N DOFs;

$\mathbf{C}_{SG} = (N \times N)$ damping coefficient and gyroscopic matrix of the rotor;

$\mathbf{K}_S = (N \times N)$ stiffness coefficient matrix containing the diagonal and cross-coupled stiffness coefficients of the shaft;

$\mathbf{x} = (N \times 1)$ vibration response vector including all degrees of freedom of the rotor with two translational and two rotational displacements at each station of the finite element;

$\mathbf{f}(\mathbf{t}) = (N \times 1)$ vector of the unbalance forces, unbalance moments, and nonlinear bearing forces.

To reduce the second-order to first-order equation system, the $(2N \times 1)$ vector \mathbf{z} of the vibration response is defined by

$$\mathbf{z} \equiv \begin{bmatrix} \mathbf{x} \\ \mathbf{y} \end{bmatrix} = \begin{bmatrix} \mathbf{x} \\ \dot{\mathbf{x}} \end{bmatrix} \Rightarrow \dot{\mathbf{z}} = \begin{bmatrix} \mathbf{y} \\ \dot{\mathbf{y}} \end{bmatrix} = \begin{bmatrix} \dot{\mathbf{x}} \\ \ddot{\mathbf{x}} \end{bmatrix} \quad (2)$$

where

$$\mathbf{y} \equiv \dot{\mathbf{x}}; \quad \dot{\mathbf{y}} \equiv \ddot{\mathbf{x}}.$$

By substituting the vector $\mathbf{z}(\mathbf{t})$ into Eq. (1), $2N$ first-order vibration equations of \mathbf{z} result in

$$\begin{aligned} \begin{bmatrix} \dot{\mathbf{x}} \\ \ddot{\mathbf{x}} \end{bmatrix} &= \begin{bmatrix} \mathbf{0} & \mathbf{I} \\ -\mathbf{M}^{-1}\mathbf{K}_S & -\mathbf{M}^{-1}\mathbf{C}_{SG} \end{bmatrix} \begin{bmatrix} \mathbf{x} \\ \dot{\mathbf{x}} \end{bmatrix} + \begin{bmatrix} \mathbf{0} \\ \mathbf{M}^{-1}[\mathbf{U}(\Omega, t) + \mathbf{F}_B(\mathbf{x}, \dot{\mathbf{x}}, t)] \end{bmatrix} \\ \Leftrightarrow \dot{\mathbf{z}} &= \begin{bmatrix} \mathbf{0} & \mathbf{I} \\ -\mathbf{M}^{-1}\mathbf{K}_S & -\mathbf{M}^{-1}\mathbf{C}_{SG} \end{bmatrix} \mathbf{z} + \begin{bmatrix} \mathbf{0} \\ \mathbf{M}^{-1}[\mathbf{U}(\Omega, t) + \mathbf{F}_B(\mathbf{x}, \dot{\mathbf{x}}, t)] \end{bmatrix} \end{aligned} \quad (3)$$

where

\mathbf{U} is the unbalance force and unbalance moment;

\mathbf{F}_B is the nonlinear bearing force, as computed by the impedance method from solving the two-phase Reynolds lubrication equation given in Eq. (11).

The coupled nonlinear vibration equation system given in Eq. (3) is written in the matrix equation of \mathbf{z} .

$$\dot{\mathbf{z}} = \mathbf{A}\mathbf{z} + \mathbf{b}(\mathbf{z}, \Omega, t) \quad (4a)$$

where

$\mathbf{A} = (2N \times 2N)$ mass, mass inertia moments, stiffness, and gyroscopic effect matrix of the rotor;

$\mathbf{b} = (2N \times 1)$ vector of the external forces and moments including unbalance and nonlinear bearing forces

within

$$\mathbf{A} = \begin{bmatrix} \mathbf{0} & \mathbf{I} \\ -\mathbf{M}^{-1}\mathbf{K}_s & -\mathbf{M}^{-1}\mathbf{C}_{SG} \end{bmatrix}; \quad (4b)$$

$$\mathbf{b}(\mathbf{z}, \Omega, t) = \begin{bmatrix} \mathbf{0} \\ \mathbf{M}^{-1}[\mathbf{U}(\Omega) + \mathbf{F}_B(\mathbf{z}, t)] \end{bmatrix}. \quad (4c)$$

The matrix \mathbf{A} containing the matrices \mathbf{M} , \mathbf{K}_s , and \mathbf{C}_{SG} is obviously non-symmetric; i.e., $\mathbf{A} \neq \mathbf{A}^T$ where \mathbf{A}^T is the transposed matrix of \mathbf{A} . In this case, the bimodal method [6] is applied to solve the first-order nonlinear matrix equation of \mathbf{z} with a large $(2N \times 2N)$ matrix \mathbf{A} of N degrees of freedom.

2.2 Two-Phase Reynolds Lubrication Equation for Oil Film Bearings

Figure 2 demonstrates a two-phase oil volume in the bearing clearances, in which the oil mixture volume V_{mix} consists of the bubble volume V_B and the liquid oil volume V_{liq} . Straightforwardly, the oil mixture volume equals the liquid oil and bubble volumes in the bearing clearance.

$$V_{mix} = V_{liq} + V_B \quad (5)$$

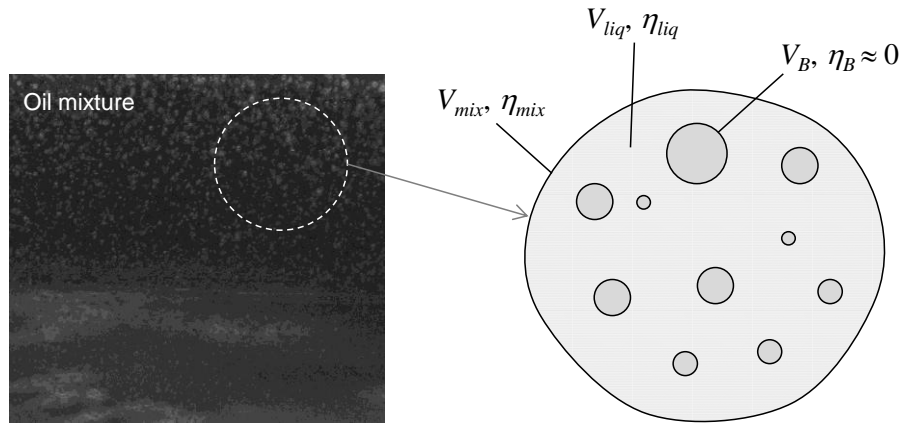


Figure 2: A two-phase oil mixture model in the bearing clearance

The oil-mixture dynamic viscosity is calculated from the liquid-oil viscosity and the bubble fraction [1, 3, 5].

$$\eta_{mix} = \eta_{liq} \left(\frac{1}{1+r} \right) = \eta_{liq} \theta \quad (6)$$

where

$r \equiv V_B/V_{liq}$ is the bubble volumetric fraction in the liquid oil that is defined by the ratio of the gas bubble volume to the oil liquid volume;

$\theta \equiv V_{liq}/V_{mix}$ is the bearing filling grade that is defined by the ratio of the liquid oil volume to the oil mixture volume. The bearing filling grade results in using Eq. (5)

$$\theta \equiv \frac{V_{liq}}{V_{mix}} = \frac{V_{liq}}{V_{liq} + V_B} = \frac{1}{1 + \frac{V_B}{V_{liq}}} = \frac{1}{1+r} \quad (7)$$

Similarly, the oil mixture density is calculated by substituting Eqs (5) and (7) at $m_B \ll m_{liq}$.

$$\rho_{mix} = \frac{m_{mix}}{V_{mix}} \approx \frac{m_{liq}}{V_{liq} + V_B} = \frac{m_{liq}}{V_{liq}(1 + V_B/V_{liq})} = \rho_{liq} \left(\frac{1}{1+r} \right) = \rho_{liq} \theta \quad (8)$$

There are two cases of the bearing filling grade: firstly, $\theta = 1$ for pure liquid oil without air-releasing or cavitation in the oil liquid; secondly, $\theta = 0$ for 100% gas phase due to air release or cavitation in oil. However, the bearing filling grade is between zero and 1 ($0 < \theta \leq 1$) in the most application cases.

Having used the Henry-Dalton's and Boyle-Mariotte's laws, the gas bubble fraction r is calculated at T and p .

$$\begin{aligned} r &\equiv \frac{V_B}{V_{liq}} = r_0 \left(\frac{Tp_0}{T_0p} \right) - a_v \left(1 - \frac{Tp_0}{T_0p} \right) \\ &= (r_0 + a_v) \left(\frac{Tp_0}{T_0p} \right) - a_v \end{aligned} \quad (9)$$

where

a_v is the Bunsen's coefficient chosen between 0.08 and 0.09 for the automotive mineral oils to 30 MPa (ISO-VG 32 to ISO-VG 220) [7]. This Bunsen solubility coefficient is defined as the maximum dissolved gas volume per unit oil liquid volume in the equilibrium condition at the air partial pressure of 101.3 kPa;

r_0 is the initial gas bubble fraction in the oil liquid at the bearing inlet;

T and p are the oil temperature and pressure in the oil film in the operating condition;

T_0 and p_0 are the ambient or oil inlet temperature and pressure.

Having substituted Eq. (9) into Eq. (7), one obtains the bearing filling grade θ as follows:

$$0 < \theta \equiv \frac{V_{liq}}{V_{mix}} = \frac{1}{(1 - a_v) + (r_0 + a_v) \left(\frac{Tp_0}{T_0p} \right)} \leq 1 \quad (10)$$

Therefore, the Reynolds lubrication equation of two-phase flow lubricating oil is written in the oil film bearings:

$$\frac{\partial}{\partial x} \left(\frac{\rho_{liq}}{\eta_{liq}} h^3 \frac{\partial p}{\partial x} \right) + \frac{\partial}{\partial z} \left(\frac{\rho_{liq}}{\eta_{liq}} h^3 \frac{\partial p}{\partial z} \right) = 6(U_r + U_b) \frac{\partial}{\partial x} (\rho_{liq} \theta h) + 12 \frac{\partial}{\partial t} (\rho_{liq} \theta h) \quad (11)$$

where

$p(x,z)$ is the current oil film pressure in the bearing clearance;

$\eta_{liq}(T)$ is the oil liquid viscosity resulting from the Cameron and Vogel's equation [2];

U_r and U_b are the circumferential velocities of the rotor and bearing ring, respectively;

$h(x)$ is the current oil film thickness in the bearing clearance;

θ is the bearing filling grade, as given in Eq. (10).

2.3 Nonlinear Bearing Forces on the Rotor

The bearing forces F_r and F_t are based on the rotating coordinate system (r, t) fixed to the journal. In fact, the bearing forces acting upon the journal in the inertial coordinate system (X_1, X_2) are required for the rotordynamic vibration equations. Therefore, the coordinate transformation from the rotating to inertial coordinate system is necessary in order to compute the bearing forces in the inertial coordinate system (X_1, X_2) , as given in Figure 3.

The radial and tangential components of the bearing force \mathbf{F}_B acting upon the rotor, opposite to the journal force \mathbf{F}_J , are resulted from integrating the oil pressure $p(x(\xi), z)$ in Eq. (11) over the journal surface.

$$\vec{\mathbf{F}}_B = \begin{bmatrix} F_r = \int_0^L R \int_0^{2\pi} p(\xi, z) \cos \xi \, d\xi \, dz \\ F_t = \int_0^L R \int_0^{2\pi} p(\xi, z) \sin \xi \, d\xi \, dz \end{bmatrix} = -\vec{\mathbf{F}}_J \quad (12)$$

within

L is the inner bearing width;

R is the journal radius;

ξ is the position angle for the oil film thickness where $x = R\xi$, as shown in Figure 3.

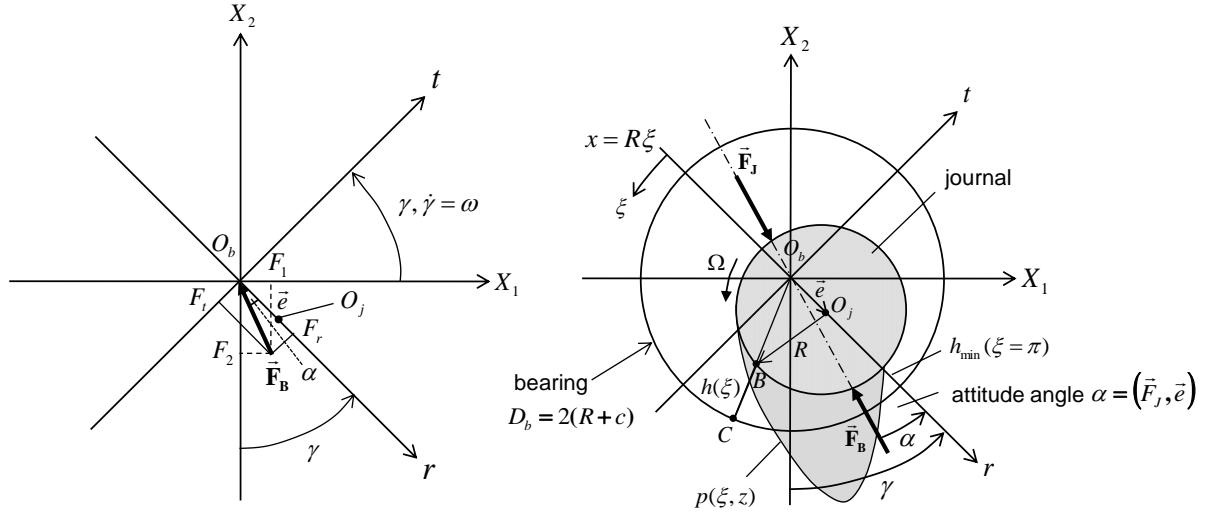


Figure 3: Bearing force components acting upon the journal

The nonlinear bearing forces in Eq. (12) are transformed into the inertial coordinate system (X_1, X_2) .

$$\bar{\mathbf{F}}_{\mathbf{B}} = \begin{pmatrix} F_1 \\ F_2 \end{pmatrix} = \begin{bmatrix} \sin \gamma & \cos \gamma \\ -\cos \gamma & \sin \gamma \end{bmatrix} \begin{pmatrix} F_r \\ F_t \end{pmatrix} \quad (13)$$

where

F_1, F_2 are the force components in the inertial coordinates X_1 and X_2 ;

F_r, F_t are the force components in the rotating coordinates r and t , fixed to the journal.

Thus, the nonlinear bearing force $\mathbf{F}_{\mathbf{B}}$ is used in the right-hand side of the rotordynamic vibration equation (3) with two components of F_1 and F_2 that depend on $\varepsilon, \gamma, \dot{\varepsilon}, \dot{\gamma}, \Omega$:

$$\bar{\mathbf{F}}_{\mathbf{B}} = \begin{bmatrix} F_1 = +F_r \sin \gamma + F_t \cos \gamma \equiv f_1(\varepsilon, \dot{\varepsilon}, \gamma, \dot{\gamma}, \Omega) \\ F_2 = -F_r \cos \gamma + F_t \sin \gamma \equiv f_2(\varepsilon, \dot{\varepsilon}, \gamma, \dot{\gamma}, \Omega) \end{bmatrix} \quad (14)$$

where

γ is the angular position of the journal;

ε is the relative eccentricity of the journal ($\varepsilon = e/c$);

c is the bearing clearance;

α is the attitude angle;

Ω is the rotor speed.

2.4 Boundary conditions for Nonlinear Rotordynamic Computations

An example of the computation of nonlinear rotordynamics for a typical automotive turbocharger using two separate rotating floating ring bearings was carried out in the study case. The following characteristics are taken into account running the rotordynamic computation program MADYN 2000 [7], which is based on the extensionally developed module for nonlinear rotordynamics of high-speed automotive turbochargers:

- run-up simulation to very high rotor speeds;
- transient behavior of the rotor responses;
- gyroscopic effect of the flexible rotor;
- two-phase oil film in the bearing clearances [1, 3];
- unbalance forces and moments acting upon the rotor;
- damping effects of the seal rings;
- nonlinear bearing forces of the rotating-floating ring bearings;
- synchronous (unbalance) and asynchronous vibrations (inner and outer oil whirls);
- rotating-floating ring bearings with changing ring speed ratios;

- computing the ring speed ratios of the bearings at each rotor speed;
- effective oil temperatures in the bearing clearances;
- heat convection in the oil films in the axial direction;
- heat conduction between the oil films in the radial direction;
- various types of lubricating oil (e.g. SAE 0W30, 5W30, 10W40, 15W40);
- various pressures and temperatures of lubricating oil at the bearing inlet.

The computed rotor of an automotive turbocharger for passenger vehicles consists of the compressor and turbine wheels, rotor shaft, thrust rings, seal rings, and rotating-floating ring bearings. One transforms this computed rotor to the discretized finite-element model (FEM) where the components of the rotor, such as the compressor and turbine wheels, rotor shaft, and radial bearings are discretized in a finite number of concentrated mass points, disks, cylinder elements, and interfaces of the bearings and seals to the rotor (s. Figure 4). The finite-element model of the computed rotor contains of many sections that are connected by the stations at both ends of each section.

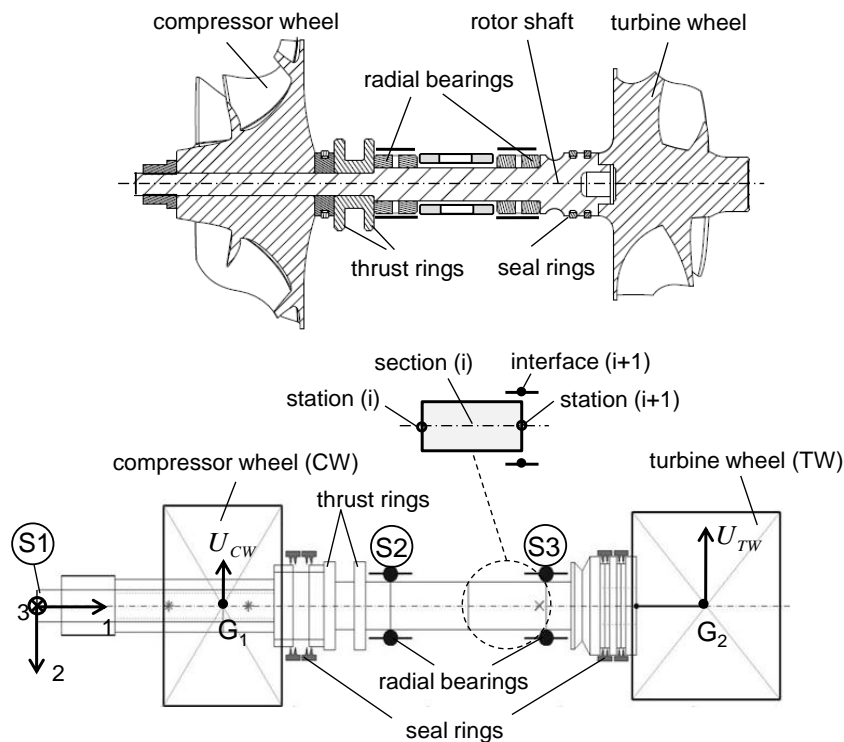


Figure 4: Computing rotor model and its discretized FEM

By solving the two-phase Reynolds lubrication equation (11) of two-oil-film bearings, the impedance table for the bearing forces is generated. The nonlinear bearing forces in the entire bearing clearance are resulted from the corresponding bearing stiffness and damping coefficients by linearly interpolating the computed values of the bearing characteristics at the position of the journal center (ε, γ) and Sommerfeld number So in the impedance table. The nonlinear bearing forces contain two force components: the rotation force induced by the rotor speed Ω depends on the bearing force angle α and $So(\eta, \varepsilon, \gamma)$; the damping force caused by the journal velocities $\dot{\varepsilon}, \dot{\gamma}$ depends on $\eta, \varepsilon, \gamma, \dot{\varepsilon}, \dot{\gamma}$ [2].

3 Results of Nonlinear Rotordynamic Computations of Turbochargers

The nonlinear bearing forces acting upon the rotor are computed at each iterating step based on the Sommerfeld number So of the impedance method. The coupled nonlinear vibration equations of the rotor are given in Eq. (3), in which we put the nonlinear bearing forces as given in Eqs (12) and (14) in the right hand side of the equation. By using the bimodal method [6], we decouple the coupled nonlinear equations in the decoupled nonlinear equations; then, the vibration responses are solved by the high-order Runge-Kutta scheme at each iterating step. By using the Discrete Fourier Transform with FFT (DFT), the frequency spectrum of the rotor responses is displayed and analyzed in the spectrogram (Waterfall diagram). The orbits of the rotor at the station S_1 of the compressor inlet, and at the stations S_2 and S_3 of the journal loci in the radial bearings are computed in the run-up simulation, as shown in Figure 4.

Two rotating floating ring bearings and two sealing rings at each side support the computed rotor with a mass of about 150 g including the shaft with a diameter of 7 mm, compressor wheel, turbine shaft, and thrust rings. The relative inner diametral clearance of the bearing is initially about 3×10^{-3} due to the temperature difference between the inner and outer oil films, the centrifugal force of the bearing ring, and the bearing ring expansion in radial direction. Hence, the relative inner diametral clearance increases to a maximum about 4×10^{-3} during operation. The ratio of the outer and inner bearing clearances is varied by a factor between 3 and 4. The maximum rotor speed is limited to nearly 225,000 rpm ($\Omega = 3750$ Hz). The compressor wheel and turbine shaft have residual unbalances of approximately 0.1 g.mm and 0.2 g.mm, respectively. The lubricating oil SAE 5W30 is used in the run-up computation; the oil dynamic viscosity changes with the effective oil film temperatures in every iterating step according to the Cameron and Vogel equation [2]. The oil condition at the inlet is given at the relative pressure of 0.3 MPa (3 bar) and oil temperature of 90°C at S2; 100°C at S3. The computing time for the run-up simulation of about 20-hour-CPU is necessary on a PC with a dual-core AMD Opteron of 3 GHz with 8 GB RAM. This computing time is quite acceptable in the industry instead of a-few-week CPU in case of instantaneously solving the Reynolds lubrication equation at each iteration step.

The vibration mode of the flexible rotor in the run-up simulation is analyzed at the stations S2 and S3. Figure 5 displays the vibration modes of the rotor at various rotor speeds. At the low speeds, the rotor vibration has a conical mode. From the rotor speed of about 81,000 rpm (36% relative rotor speed) to 135,000 rpm (60% relative rotor speed), the rotor vibration changes from the conical to cylindrical mode.

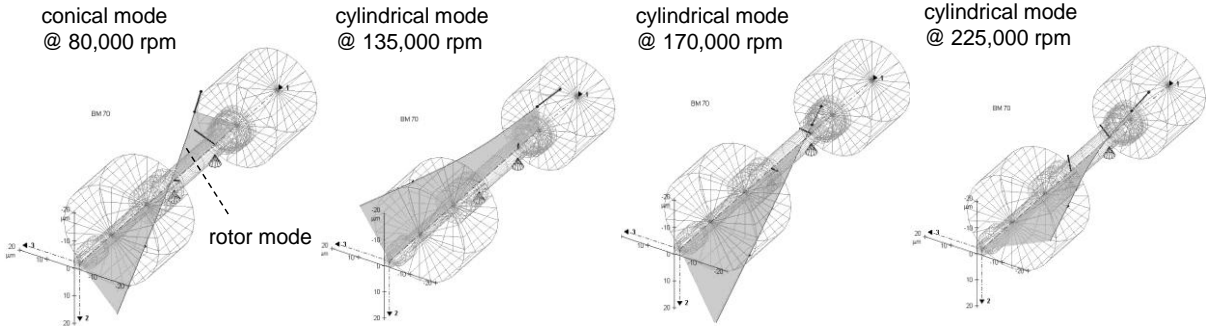


Figure 5: Vibration modes of the turbocharger rotor [2, 3]

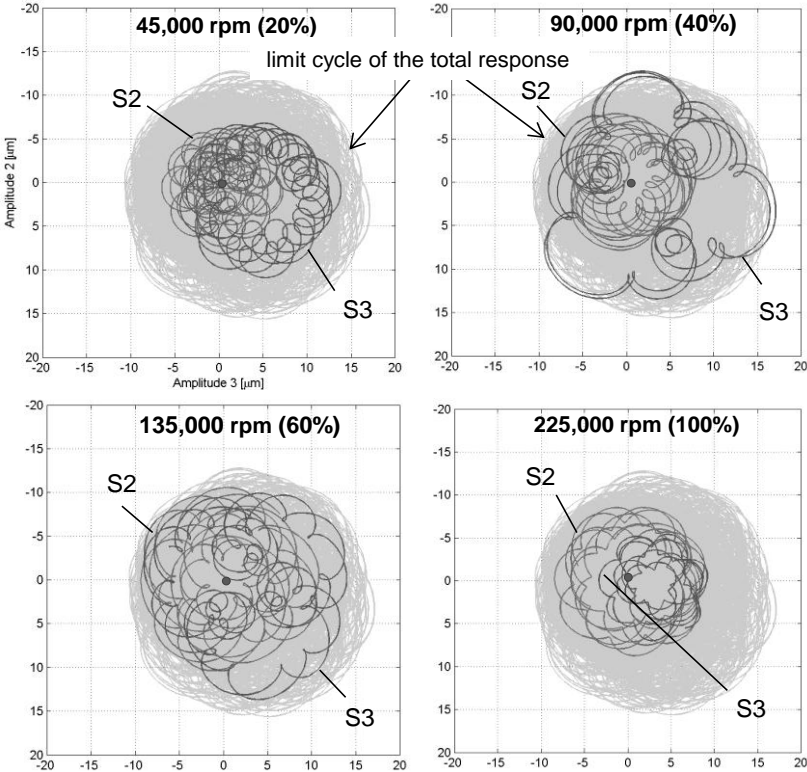


Figure 6: Orbit of the journal at the stations S2 and S3

At low rotor speeds up to nearly 45,000 rpm, the rotor orbits at S2 and S3 are mostly eccentric to each other (s. Fig. 6), i.e. the mode shape of the rotor response is conical since the rotor is still rigid at low rotor speeds. At high rotor speeds from about 81,000 rpm, the bearing stiffness and damping coefficients increase, the conical mode of the rotor vibration tends toward cylindrical mode. Figure 6 shows that orbits at S2 and S3 are nearly concentric from the relative speed of 60% up to the maximum rotor speed. The limit cycles of the rotor response at S2 and S3 have peak-to-peak amplitude of about 25 μm at 135,000 rpm and reduce to 15 μm at the maximum rotor speed of 225,000 rpm.

The unbalance amplitude (1X) is relatively small compared to the asynchronous amplitudes of the inner and outer oil whirls in the entire rotor speed range. In fact, the typical resonance due to unbalance does not exist in nonlinear rotordynamics (s. Figures 7, 8a, and 8b), but only the limit cycle of the rotor response occurs at each rotor speed. The reason is that the effective stiffness coefficient of the rotor depends not only on the stiffness coefficient of the rotor shaft itself but also on the bearing stiffness coefficient; the equivalent stiffness coefficient of the rotor is called the non-synchronous complex dynamic stiffness. In turn, the bearing stiffness coefficient is dependent of the effective oil pressure, temperature, rotor speed, bearing ring speed, and journal eccentricity as well. At large rotor deflections, the journal eccentricity increases in the bearing clearance; the oil-film thickness reduces in the clearance. Therefore, the stiffness and damping coefficients of the bearing increase with the rotor deflection until the journal orbit stabilizes in the limit cycle at each rotor speed after the Hopf bifurcation point [2]. In this case, no typical resonance like in linear rotordynamics occurs in the entire rotor speed range, as shown in the Waterfall plot (s. Figure 7).

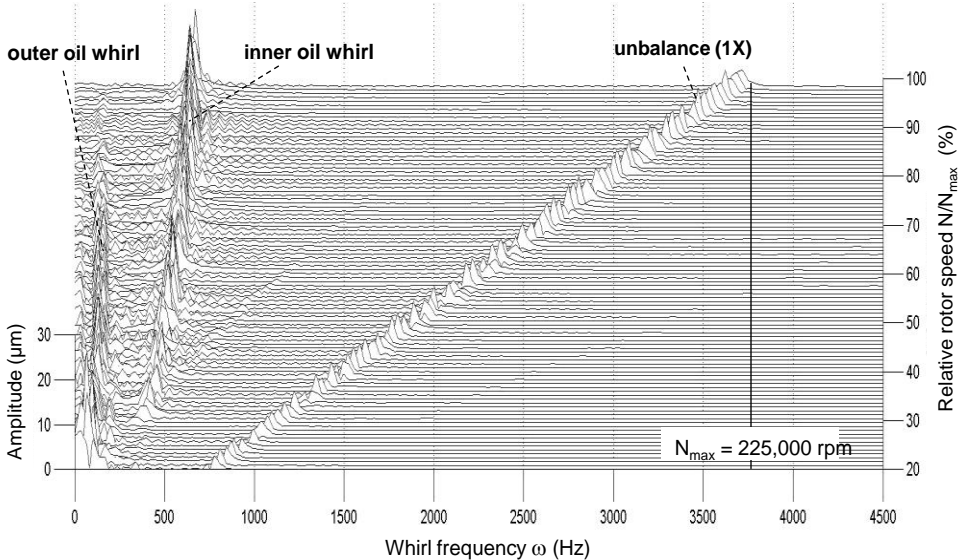
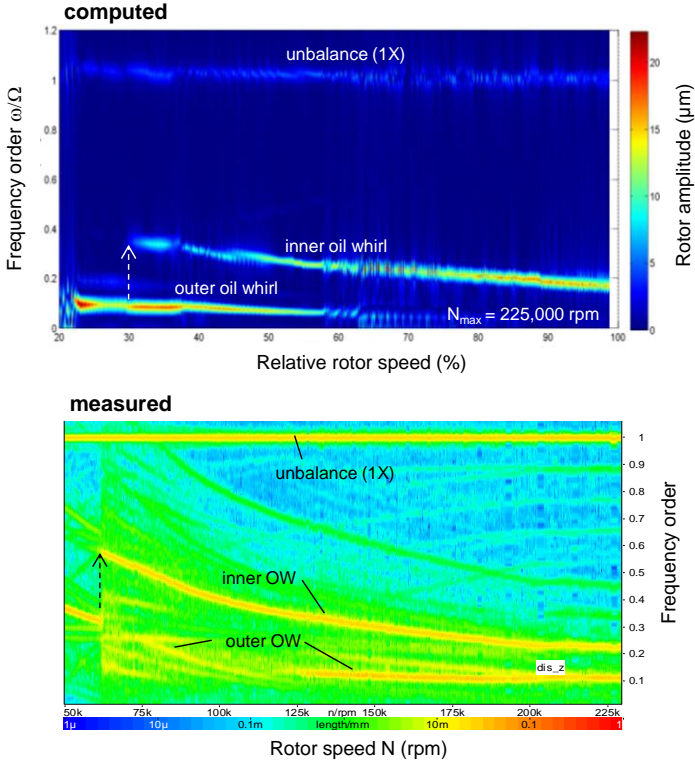


Figure 7: Waterfall plot of the journal at the station S1

In practice, one plots Waterfall diagram in a two-dimensional plot (called modified Waterfall plot), in which the amplitudes of the vibrations are displayed in the color or gray scale in the frequency-order spectra, as shown in Fig. 8a. Instead of the whirl frequency ω , the frequency order ω/Ω vs. rotor speed Ω is used in the modified Waterfall plot with the advantage to easier analyze the frequency-order spectra of the synchronous and asynchronous vibrations versus the rotor speed in the abscissa. The frequency jump of the inner oil whirl takes place at nearly 30% of relative rotor speed, where the conical vibration mode changes into the cylindrical mode.

Figures 8a and 8b show the comparison between the computation of rotordynamics and measurement results in Waterfall plots. Compared to the measurement, the computed inner oil whirl takes place a little later at the relative rotor speed of about 30% (67,500 rpm) instead of at nearly 27% (62,000 rpm) at the measurement. The frequency order of the computed inner oil whirl (inner OW) begins at a lower frequency order of 0.4X compared to about 0.55X in the measurement and ends at the frequency order of 0.2X, nearly the same as in the measurement results. The low frequency order of the inner oil whirl is caused by the higher bearing ring speed in the measurement than in the computation. The unknown heat flow transferred from the bearing housing to the outer oil film of the bearing has not been taken into account in the computation. As a reason, the outer oil film temperature increases in the measurement compared to the computation; therefore, the ring speed ratio of the bearing is higher, leading to the higher frequency order of inner oil whirl. In fact, the residual unbalance vectors in the compressor and turbine wheels are unknown after trim balancing. As a reason, the resulting residual unbalance may be smaller in the computation. Thus, the frequency jump of inner oil whirl occurs at a relative rotor speed of about 67,500 rpm a little later than in the measurement at 62,000 rpm. Similarly, the computed frequency order of the outer oil whirl (called outer OW) is a little lower than the frequency order as in the

measurement due to the reduced bearing ring speed, especially at low rotor speeds. Note that the inner oil whirl causes the constant tone, a subsynchronous self-excited rotor response; the rotor unbalance generates the unbalance whistle. These noises are transmitted via the periphery components neighboring the turbocharger and as well as through the car frame into the air-borne noises occurring in the passenger vehicle cabin [3, 4].



Figures 8a and 8b: Waterfall plots of the journal at the station S1

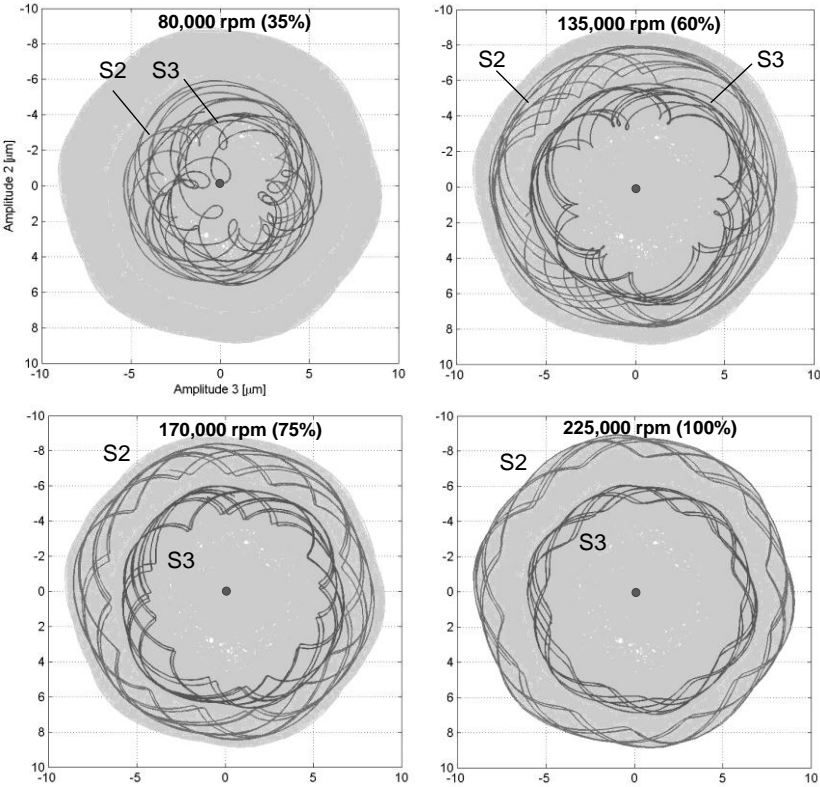


Figure 9: Waterfall plots of the relative displacements between the journal and bearing ring at the stations S2 and S3

In the rotating floating ring bearing case, the journal moves relatively to the bearing ring at every rotor speed; i.e., the journal motion moves the bearing ring in the radial direction. In practice, it is very difficult to measure the relative displacements between the journal and bearing ring during rotation. Hence, the rotordynamic computation is a useful tool to determine the relative displacements and the current oil-film thickness in the rotating floating ring bearings at any rotor speed. Figure 9 displays the relative displacements between the journal and bearing ring at various rotor speeds. At the beginning, the journal and bearing ring are nearly concentric to each other since the rotor mass is very small at nearly 150 g. If the relative displacement is positive, the journal moves closer to the bearing ring because the journal displacement is larger than the ring displacement. In the other case the journal moves away from the bearing ring. The current oil-film thickness is resulted from the bearing clearance and relative displacement. When the oil-film thickness is larger than the limit oil-film thickness [2], the lubrication regime is fully hydrodynamic and outside the mixed and boundary lubrications; no or little wear occurs in the bearing. The computed results show the maximum relative displacement is about 9 μm in the limit cycle for the entire rotor speed range. It indicates that the minimum oil-film thickness in the inner bearing clearance is nearly 5 μm with the inner radial clearance of 14 μm . The minimum oil-film thickness of 5 μm in the bearing clearance is larger than the limit oil-film thickness; hence, no wear occurs in the bearing.

4 Conclusions

Generally, the boundary conditions are assumed as ideal in the rotordynamic computation, such as sufficient supply oil, real oil temperature at the bearing inlet, foamy oil, residual unbalance vectors, good parallelism of the thrust bearing, all wedges of the thrust bearing having the same slope, good quality of the radial bearing in terms of the bearing non-coaxiality, surface roundness, and characteristics of surface roughness. In fact, such ideal boundary conditions do not usually exist due to mass production in automotive turbochargers. The unknown or uncertain boundary conditions strongly affect the stability and functionality of the rotor. Unfortunately, it is very difficult or impossible to take all of them into account in the rotordynamic computation where only the rotor containing the compressor, turbine wheels, rotor shaft, radial bearings, and seal rings is considered. Therefore, the rotordynamic computation cannot cure the instability and malfunctions of the rotor, or prevent it from damage at additional inappropriate oil conditions and qualities, such as oil insufficiency, contaminated oil with hard particles, foamy oil, and oil coking in the bearing clearances during the operation.

However, the computational results help us better understanding the rotor responses and give quick ideas how to improve the turbocharger behavior. Additionally, experimental measurements also provide us with the real rotor response at such unknown boundary conditions that could not be considered in the computation. Therefore, the combination method between the rotordynamic computation and experimental measurements has been generally used in further improvements of rotor stability and reduction of bearing friction of automotive turbochargers.

Acknowledgement

The author is indebted to his colleague, Mr. Daren Bolbolan, for reviewing this paper and giving constructive recommendations.

References

- [1] Bartel, D. (2010): *Simulation von Tribosystemen*. Springer-Teubner
- [2] Nguyen-Schäfer, H. (2012): *Rotordynamics of Automotive Turbochargers*. Springer, Berlin-Heidelberg
- [3] Nguyen-Schäfer, H. (2013): *Aero and Vibroacoustics of Automotive Turbochargers*. Springer, Berlin-Heidelberg
- [4] Nguyen-Schäfer, H. and Kleinschmidt, R. (2012): *Analysis and Nonlinear Rotordynamics Computation of Constant Tone in Automotive Turbochargers*. 17. ATK Conference, Dresden, Germany
- [5] Nguyen-Schäfer, H. and Sprafke, P. (1997): *Numerical Study on Interaction Effects of the Bubbles induced by Air-Release and Cavitation in Hydraulic Systems*. 10. Bath International Fluid Power Workshop, Bath; UK. Research Studies Press Ltd., Hertfordshire, England
- [6] Nordmann, R. (1976): *Schwingungsberechnung von nichtkonservativen Rotoren mit Hilfe von Links- und Rechts-Eigenvektoren*. VDI Bericht 269
- [7] Schmied, J. (2012): *Program MADYN 2000 for Computation of Rotordynamics*, Delta J.S., Zurich.